ACS SENSORS

Editors' Choice

pubs.acs.org/acssensors

Article

3D-Printed CNT-Reinforced Bioresorbable Vascular Scaffold with Enhanced Mechanical Stability and Integrated Wireless Pressure Sensor for Continuous Hemodynamic Monitoring

Nomin-Erdene Oyunbaatar, Jinliang Wei, Lei Wang, Su-Hwan Kim, Heonzoo Lee, Kyeongha Kwon, Yonggwan Won, and Dong-Weon Lee*

Cite This: https://doi.org/10.1021/acssensors.5c00857

Read Online

ACCESS | Metrics & More | Article Recommendations | Supporting Information

ABSTRACT: Polymer-based bioresorbable vascular scaffolds (BVS) have garnered significant attention in biomedical applications. Among various BVS, polycaprolactone (PCL)-based scaffolds exhibit excellent biocompatibility, flexibility, chemical stability, and controlled degradation. However, their low radial strength limits practical applicability. Moreover, most reported BVS require periodic postimplantation monitoring to enable early detection of in-stent restenosis and thrombosis. To overcome these limitations, we fabricate a carbon nanotube (CNT)-reinforced PCL BVS using a 3D printing process, enabling patient-specific customization while significantly improving mechanical strength and durability. The proposed PCL/CNT-based stent not only serves as a structural scaffold but also facilitate real-time vascular pressure monitoring by integrating a wireless LC capacitive pressure sensor. The LC pressure sensor is microfabricated using microelectromechanical systems (MEMS) technology and exhibits highly stable resonance characteristics. A key innovation is the integration of a supporting micropillar within the capacitor cavity, which minimizes structural deformation and ensures a stable capacitance response. Mechanical testing demonstrates that PCL/CNT stents achieve significantly higher radial force (0.1 N/mm) compared to pristine PCL (0.013 N/mm). The wireless sensor exhibits high sensitivity (49 kHz/mmHg) with minimal capacitance variation (±5%). *In-vitro* studies in a phantom experiment confirm stable resonance frequency fluctuations that accurately correlate with hemodynamic changes. This smart stent integrates biodegradable nanocomposites, 3D printing, and wireless sensing, providing a noninvasive platform for restenosis and thrombosis monitoring. It marks a significant advancement in cardiovascular implants, paving the way for personalized and proactive patient care.

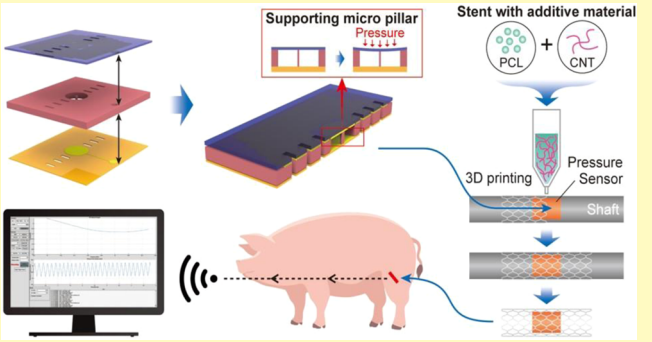

KEYWORDS: *PCL/CNT hybrid nanocomposite, 3D-printing, bioresorbable vascular scaffolds, structurally reinforced capacitive sensor, wireless LC pressure sensor, hemodynamic monitoring*

Percutaneous coronary intervention (PCI) is a widely adopted minimally invasive technique for treating coronary artery disease (CAD) by restoring blood flow in occluded arteries.[1−4] The underlying pathology of CAD is atherosclerosis, characterized by the progressive accumulation of plaque within arterial walls, leading to restricted blood flow. Stenting remains the most effective intervention, with over 954,000 PCI procedures performed annually in the United States.[5] Traditional metallic stents, including bare-metal and drug-eluting stents, have significantly reduced acute vessel closure rates and improved clinical outcomes.[6−8] However, long-term complications such as in-stent restenosis, late stent thrombosis, and imaging artifacts in computed tomography and magnetic resonance imaging continue to pose challenges.[9,10] These limitations necessitate the development of alternative materials with enhanced performance and biocompatibility.

Bioresorbable vascular scaffolds (BVS) made from biodegradable polymers like poly(L-lactic acid) (PLLA), polyglycolic acid (PGA), and polycaprolactone (PCL) have gained significant attention. These materials provide temporary mechanical support and gradually degrade, allowing the blood vessel to restore its natural function.[11−14] Among these polymers, PLA has higher strength and stiffness than PCL and degrades more slowly than PLGA.[15] This makes PLA a promising biodegradable material for fabricating BVS for

Received: March 15, 2025
Revised: July 17, 2025
Accepted: July 18, 2025

various medical applications.[16] However, using PLA for cardiovascular stents is challenging due to its brittleness.[17,18] On the other hand, PCL-based BVS offers a good balance between mechanical strength and controlled degradation.[19,20] However, a key drawback of PCL-based BVS is their low radial strength, which limits their ability to keep blood vessels open until complete vascular remodeling occurs.[21−23]

Recently, several strategies have been explored to enhance the radial force of PCL stents, including the incorporation of reinforcing agents such as gelatin and hydroxyapatite.[24−26] For example, Guerra et al. developed a heterogeneous polymer composite based on a PCL/PLA cardiovascular scaffold, which exhibited enhanced mechanical properties.[27] However, processing PLLA using 3D printing or casting techniques remains constrained by its inherent brittleness. Carbon-based materials, such as graphene, carbon quantum dots, and CNTs, have been incorporated into PCL to improve its mechanical properties.[28−30] For instance, Misra et al. proposed patient-specific stenting by utilizing direct 3D printing of a PCL-graphene platelet composite, which exhibited improved mechanical strength.[28] CNTs, in particular, have been widely studied due to their exceptional mechanical strength, electrical conductivity, and biocompatibility.[29−31] Several studies have demonstrated that PCL-CNT composites significantly improve tensile strength and durability, addressing the inherent mechanical weaknesses of PCL scaffolds.[32,33] However, most of the reported PCL/CNT composite scaffolds have been explored in tissue engineering rather than direct stent applications. Furthermore, traditional scaffold manufacturing techniques often fail to provide the necessary customization for patient-specific stenting, further limiting their clinical success.

To address the challenges associated with patient-specific stenting, 3D printing has emerged as a promising technique for fabricating complex and customized vascular scaffolds.[34,35] By directly segmenting medical images, patient-specific stents can be designed and 3D printed using PCL-based composites reinforced with CNTs, improving their strength and durability. Beyond structural support, continuous monitoring of vascular pressure postimplantation is crucial for early detection of in-stent restenosis and thrombosis, conditions that pose serious risks to patient health. Conventional pressure measurement methods, such as catheter-based techniques, are highly invasive and unsuitable for long-term monitoring. Recent advances in wireless sensing technology have enabled the development of LC-based pressure sensors, which offer a noninvasive approach to real-time hemodynamic monitoring.[36−40] However, existing LC sensors often suffer from structural deformations due to the thermal bonding process, leading to signal instability and inaccurate pressure readings. These limitations hinder clinical applicability, emphasizing the need for design modifications that enhance the sensor's mechanical robustness and signal reliability.

Herein, we propose a PCL/CNT hybrid BVS fabricated using advanced 3D printing technology. The integration of CNTs within the PCL matrix enhances tensile strength, durability and effectively addresses the inherent mechanical weaknesses of polymer-based stents. Compared to pristine PCL and PLA-based BVS, the PCL/CNT composite BVS exhibits significantly enhanced radial force, ensuring improved vascular support and stability. Beyond structural reinforcement, the stent incorporates a wireless LC pressure sensor for continuous hemodynamic monitoring. To successfully mitigate structural deformation, present in reported wireless LC pressure sensors, a supporting micropillar structure is strategically integrated within the capacitor cavity area, effectively reducing diaphragm deformation and ensuring a stable capacitance response under physiological conditions. In vitro evaluations, including mechanical characterization, pressure sensitivity analysis, and wireless signal stability assessments, have demonstrated the feasibility of the proposed stent in practical applications. This approach represents a significant advancement in bioresorbable vascular scaffold technology by combining biodegradable nanocomposites, patient-specific 3D printing, and real-time wireless sensing, paving the way for next-generation smart stents that not only provide temporary vascular support but also enable continuous, noninvasive health monitoring.

MATERIAL AND METHODS

Materials. Silicon wafers (4-in.) were obtained from Silicon Technology Cooperation (Korea). SU-8 3010 and PermiNex 1000 were sourced from Kayaku Advanced Materials. The photosensitive resist AZ4620 and buffered oxide etchant (BHF) were purchased from MicroChemicals (Germany). Polycaprolactone (PCL, Mw 80,000), carbon nanotubes (CNT) and dimethylformamide (DMF) were obtained from Sigma-Aldrich.

PCL and CNT Reinforced PCL BVS Fabrication. The fabrication of both pristine PCL and CNT-reinforced PCL composites at varying weight fractions (0.1, 0.2, 0.5, 1, and 2%) (Figure S1) was conducted using a precisely controlled FDM (fused deposition modeling) 3D printing process. Initially, CNTs were dispersed into 10 mL of DMF and subjected to magnetic stirring at 80 °C for 2 h to achieve homogeneous dispersion. To further enhance uniformity, PCL was subsequently introduced into the CNT dispersion, followed by ultrasonic treatment to facilitate the formation of a well-integrated polymer nanocomposite (Figure S2). To eliminate residual solvent, the DMF was removed by employing a drying process, utilizing a hot plate and left overnight to ensure complete solvent evaporation. The prepared composite material was extruded at a precisely controlled pressure of 0.5 MPa and a speed of 3 mm/s, with the container temperature maintained at 160 °C to ensure optimal flow characteristics during printing. Notably, PCL melt exhibits Newtonian fluid behavior, with its viscosity primarily dependent on temperature.[41] For accurate deposition, a specialized print head equipped with a dispensing nozzle featuring an inner diameter of approximately 200 μm was employed. The FDM-based printing approach allowed direct and precise fabrication of the stent structure onto the print bed while ensuring geometric accuracy. Through systematic optimization of the printing parameters, the stents were fabricated with a uniform thickness of 150 μm and a width of 225 μm. The printing process was carried out on a cylindrical shaft with a diameter of 2.75 mm to provide structural stability. The final stents achieved an outer diameter of 3.05 mm and a length of 18 mm, meeting the dimensional specifications required for cardiovascular applications.

LC Pressure Sensor Fabrication. The fabrication of the LC resonance-type wireless pressure sensor follows a meticulously controlled microfabrication process, involving the sequential development of the capacitor layer, inductor coil layer, and their final assembly (Figure S3). Initially, a 300 nm thick silicon dioxide (SiO_2) layer is thermally grown on a 4-in. silicon wafer through a wet oxidation process at 1000 °C for 40 min, serving as a sacrificial layer for the eventual release of the sensor. A 10 μm thick SU-8 3010 base layer is then spin-coated onto the SiO_2 substrate at 2400 rpm for 40 s. Subsequently, a 10 nm thick titanium (Ti) adhesion layer and a 100 nm thick chromium (Cr) conductive layer are deposited using DC sputtering at 50 W for 1 h to form the capacitor electrodes. The capacitor structure, with varying diameters (400−1300 μm), is defined through a metal wet etching process. A 2 μm thick SU-8 insulating layer is then spin-coated and patterned to encapsulate the capacitor electrodes, leaving a small opening for electrical

https://doi.org/10.1021/acssensors.5c00857
ACS Sens. XXXX, XXX, XXX−XXX

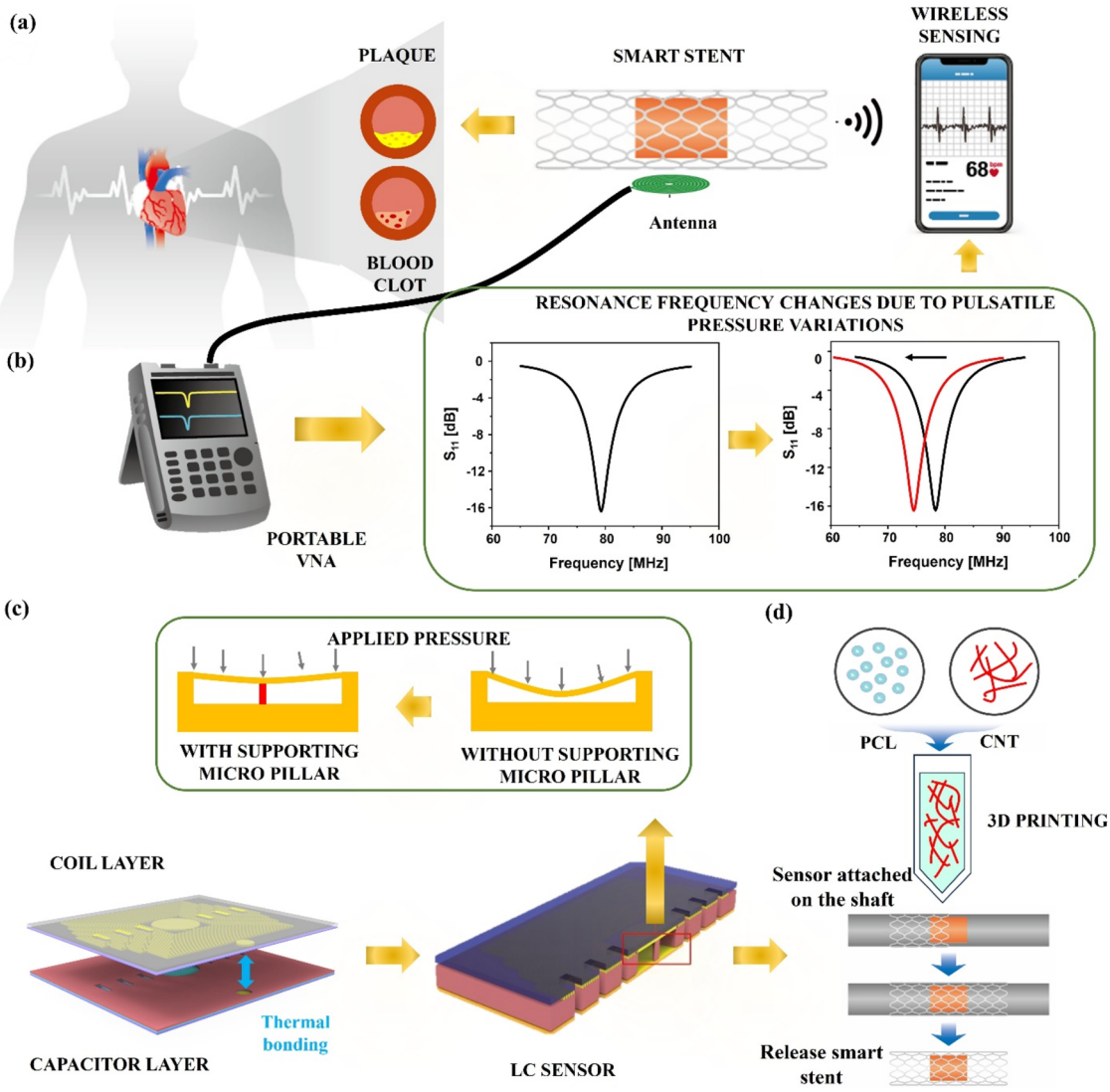

Figure 1. Schematic of the smart stent. (a) Schematic illustration of the CNT-incorporated smart stent and its wireless sensing mechanism. (b) Measurement setup showing resonance frequency changes due to pulsatile pressure variations using a portable vector network analyzer (VNA). (c) Supporting micropillar-integrated LC wireless pressure sensor designed to enhance mechanical stability and sensing performance under applied pressure. (d) Schematic of the 3D printing process for integrating the LC pressure sensor with the CNT-incorporated stent to produce the smart stent.

connections. To enhance sensor performance, multiple capacitor cavity layers (1300, 800, and 400 μm in diameter) are patterned. A supporting microstructured pillar, with a diameter set to 10% of the capacitor's initial diameter, is introduced at the center of the capacitor plate to mitigate mechanical deformation during bonding. For the fabrication of the inductor coil layer, a thick AZ4620 positive photoresist mask (12 μm) is applied to define the coil structure, followed by gold (Au) electroplating (10 μm thickness) to ensure high electrical conductivity. A gold (Au)-electroplated inductor coil, designed with 24 precise turns, is perpendicularly aligned with the capacitor layer, a crucial design feature that optimizes electromagnetic performance and signal transmission efficiency. Each coil turn has a coil width of 0.03 mm and a pitch distance of 0.03 mm, ensuring high conductivity and resonance stability. A 35 μm thick SU-8 encapsulation layer is then coated and patterned over the inductor coil to provide structural protection. To facilitate sensor release, a 10 μm thick PermiNex layer is spin-coated onto the SU-8 encapsulation layer, providing an air cavity and additional electrical connection points. The final capacitor plate layer is then released from the silicon wafer by dissolving the SiO_2 sacrificial layer using a buffered hydrofluoric acid (BHF) solution. For sensor assembly, the capacitor and inductor coil layers are precisely aligned in a perpendicular configuration to optimize capacitive sensing performance. The final integration is achieved through a thermal bonding process at 150 °C for 1 min, ensuring stable adhesion and reliable sensor operation.

Fabrication of Smart Stent. The integration of the LC resonance-type wireless pressure sensor with the PCL or PCL/CNT nanocomposite stent followed a systematic fabrication approach to ensure seamless incorporation and optimal performance (Figure S4). Initially, the LC pressure sensor was attached to a 3D-printed shaft using a poly(vinyl alcohol) (PVA) water-soluble solution, which acted as a temporary adhesion layer to support the subsequent stent printing process. Following this, the PCL or PCL/CNT composite stent was printed directly onto the sensor. Using a high-precision 3D-printing technique, the stent was printed with a filament width of 200 μm, as discussed in the earlier section. To achieve uniform CNT dispersion and maintain printability, various CNT weight fractions were explored, and an optimal concentration was selected. Once the stent structure was successfully printed, the sacrificial PVA layer was dissolved in water, allowing for the gentle detachment of the stent-integrated sensor also known as smart stent from the 3D-printed shaft. During 3D-printing process, the molten composite material

https://doi.org/10.1021/acssensors.5c00857
ACS Sens. XXXX, XXX, XXX−XXX

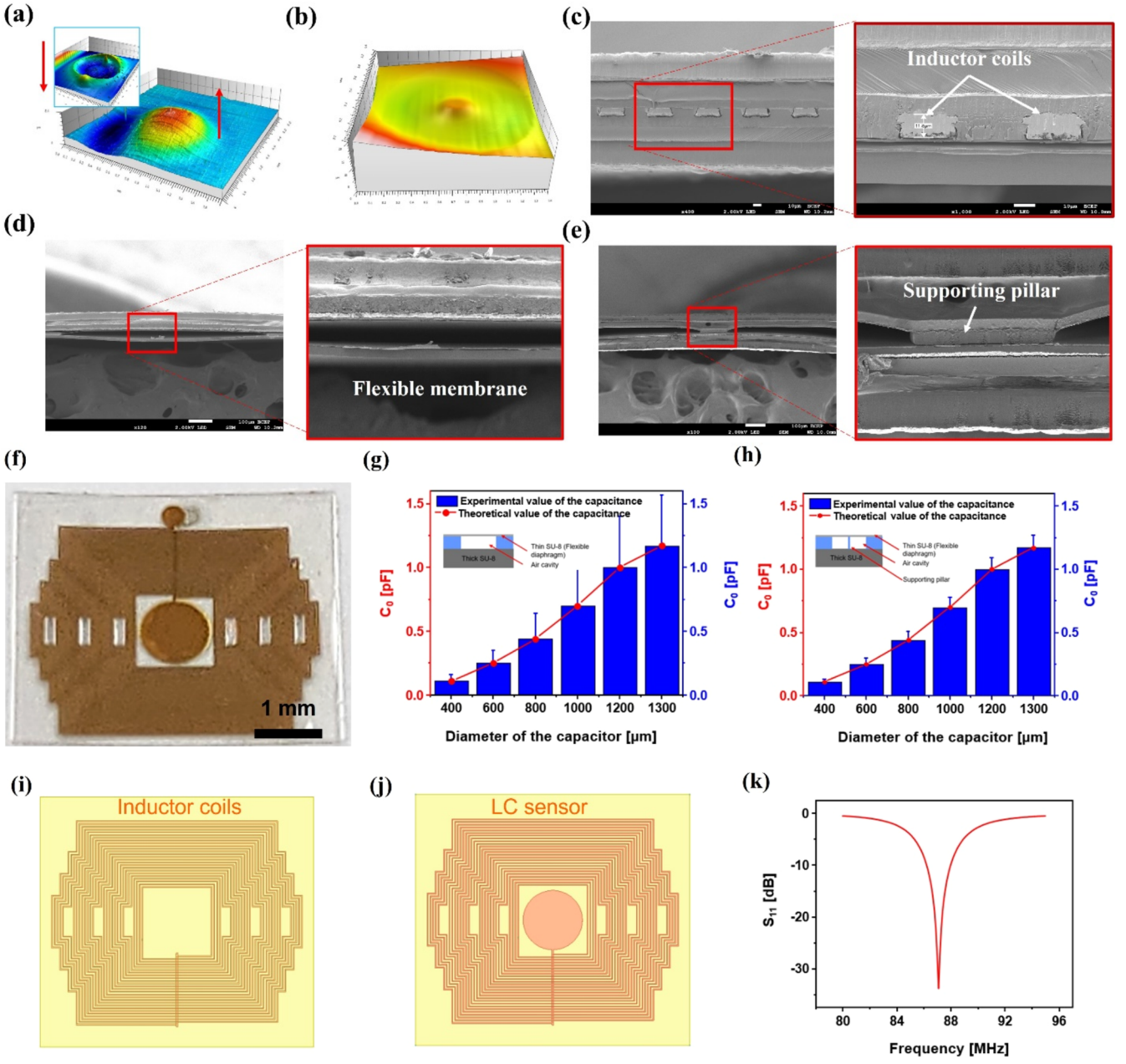

Figure 2. Structural morphology and initial characterization of the LC pressure sensor. (a, b) 3D surface morphology of the LC sensor after thermal bonding, shown without and with a supporting micropillar. (c) Cross-sectional FE-SEM image displaying the inductor coil structures of the LC pressure sensor. (d, e) Cross-sectional SEM images of the capacitor cavity, illustrating the structural comparison without and with a supporting micropillar. (f) Optical image of the fabricated LC pressure sensor. (g, h) Comparison of theoretical and experimental capacitance values for different capacitor diameters. (i, j) Simulation layouts of the inductor coil and the integrated LC sensor. (k) Resonance frequency response (S_1) of the LC sensor.

penetrated the open structure of the sensor, forming a strong mechanical interlock between the sensor and the stent (Figure S5).

Equipment Utilized for Characterization of the Sensor. The cross-sectional view of the LC sensor was analyzed using field emission scanning electron microscopy (FE-SEM, JSM-7900F; JEOL). The radial force of the fabricated stents was evaluated using a universal tensile testing machine (EZ-L; Shimadzu, Japan). The inductance of the LC pressure sensor was measured using an LCR meter (E4980AL; KEYSIGHT). The resonance characteristics of the smart sensor were examined inside a pressure chamber (MMVC2S_S/4P, MSTECH). Pressure variations were controlled using a syringe pump (LEGATO 210, kd Scientific) and monitored with a pressure gauge. The resonance frequency was recorded using a network analyzer (N9913B; KEYSIGHT).

RESULTS AND DISCUSSION

Figure 1A illustrates the operational principle and assembly process of the PCL/CNT BVS with an embedded LC wireless pressure sensor. The CNT-incorporated smart stent functions as a wireless hemodynamic monitoring system, detecting vascular pressure changes caused by plaque formation or blood clot-induced stenosis. To validate this function, the measurement was carried out using a portable network analyzer with an external coil antenna to detect the resonance frequency shift caused by pulsatile pressure variations, as illustrated in Figure 1B. Figure 1C illustrates the LC wireless pressure sensor, which consists of two primary functional layers: a capacitor

https://doi.org/10.1021/acssensors.5c00857
ACS Sens. XXXX, XXX, XXX−XXX

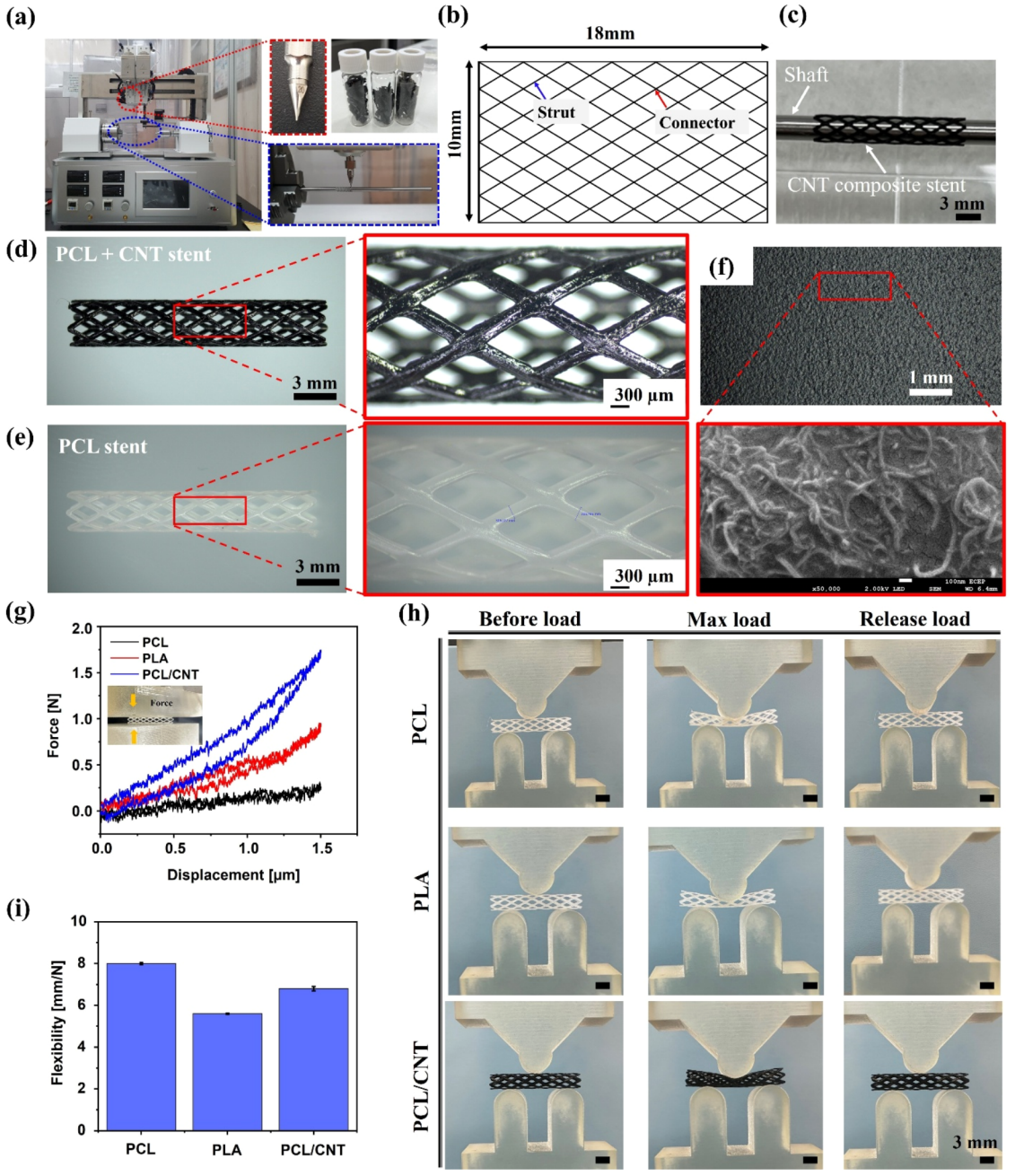

Figure 3. Fabrication and mechanical characterization of the PCL/CNT BVS. (a) Photograph of the 3D printing setup and PCL/CNT composite material used for fabrication of BVS. (b) Schematic representation of the stent design. (c) Printed PCL/CNT BVS on the printing shaft. (d, e) Optical images of the 3D printed PCL/CNT and PCL BVS. (f) FESEM images showing the distribution of CNTs within the PCL matrix. (g) Force−displacement curves of PCL, PLA, and PCL/CNT BVS. (h) Three-point bending test of the stents under different loading conditions. (i) Flexibility comparison of PCL, PLA, and PCL/CNT stents.

layer that detects pressure variations via capacitance changes and an inductor coil layer that facilitates wireless inductive coupling, ensuring efficient signal transmission to the external coil antenna. During the assembling two layers of the sensor, thermal bonding at 150 °C for 1 min induces polymer capacitor deformation due to air expansion within the cavity, causing diaphragm displacement and potential sensor misalignment. Ideally, the diaphragm should deflect inward in response to external pressure, maintaining a precise gap to ensure accurate capacitance measurements. However, during the hot press bonding of the capacitor and inductor layers, trapped air within the cavity expands at elevated temperatures, resulting in uncontrolled upward or downward displacement of the diaphragm, which can alter the intended electrode spacing and baseline capacitance, compromising measurement accuracy.

To address this issue, a micro support pillar is strategically incorporated at the center of the capacitor plate, with a diameter set to 10% of the capacitor's initial diameter. This structure prevents excessive diaphragm deflection, maintaining a uniform distance between the capacitor plates and preserving sensor accuracy and reliability. The fabricated LC sensor exhibits an overall compact footprint of 6.5 × 6.5 mm^2, making it suitable for implantation within vascular structures. As the

https://doi.org/10.1021/acssensors.5c00857
ACS Sens. XXXX, XXX, XXX−XXX

capacitor deforms in response to pressure fluctuations, its capacitance changes, leading to a shift in resonance frequency, which is then wirelessly transmitted to an external monitoring system for real-time vascular assessment. In Figure 1D, the PCL/CNT BVS was 3D-printed onto a shaft where the LC pressure sensor was attached, ensuring structural integration and enhanced mechanical strength. Figure S6 illustrates micromachined sensor components fabricated using MEMS technology on a silicon substrate, integrating both capacitive and inductive elements. The optical images depict arrays of flexible capacitive sensor structures and inductor coil components, highlighting the batch fabrication approach for miniaturized sensing devices (Figure S6A,d). Figure S6B,c shows the capacitor structures, deposited over a silicon oxide layer. Figure S6E,f provides detailed images of the electroplated inductor coils, featuring a Ti/Au conductive layer encapsulated within SU-8 2002, ensuring high electrical conductivity and structural integrity.

Figure 2A shows the 3D surface profile images illustrating the undesirable deflection of the flexible capacitors caused by air expansion during the hot-press bonding process. This unintended deformation introduces variations in the sensor's output, known as initial tolerance, complicating calibration and reducing measurement accuracy. To mitigate these issues, a microstructured pillar was strategically positioned at the center of the capacitor plates, effectively stabilizing the flexible capacitor within a controlled operational range (Figure 2B). Figure 2c displays a cross-sectional SEM image of the encapsulated inductor coils, revealing a uniform thickness of 10 μm. To ensure this uniformity, AZ4620 positive photoresist was patterned onto the Au-deposited surface before electroplating, which was conducted under a fixed current of 0.08 A for 30 min. Following electroplating, the photoresist was removed, yielding a well-defined inductor coil and thick capacitor plates (Figure S7A). Figure 2D,e provides SEM cross-sectional views of the capacitor plates without and with the supporting micropillar, respectively. The presence of the supporting micropillar prevents direct contact between the top and bottom capacitor plates during thermal bonding and mitigates misalignment caused by sudden cooling due to air expansion. The micropillar effectively maintains uniform spacing in the central region of the capacitor, reducing upward or downward deflection of the plates and thereby improving the sensor's mechanical and electrical stability. Figure 2F shows the optical image of the fabricated sensor. Figure S7B,C depicts micropatterned capacitor structures with and without the supporting micropillar, respectively.

The initial capacitance of the capacitor was evaluated by varying diameters (400, 600, 800, 1000, and 1300 μm) without and with micropillar structure, as shown in Figure 2G,h. The LC sensor's wireless signal detection is based on the relationship between capacitance (C) and inductance (L), which is theoretically defined by $f_r = \frac{1}{2\pi\sqrt{LC}}$ where f_r represents the resonance frequency, primarily influenced by capacitance variations. When external pressure is applied, the capacitor's physical dimensions or dielectric properties change, resulting in a capacitance shift and, consequently, a resonance frequency variation. To quantify the impact of the supporting micropillar, the initial capacitance was measured for capacitors of different diameters. The experimental data indicate that capacitors without a supporting pillar exhibited significantly higher capacitance tolerance, with deviations reaching up to ±15% for larger diameters. In contrast, capacitors with an integrated micropillar demonstrated a marked reduction in capacitance variation, with tolerance limited to ±5%, highlighting its effectiveness in maintaining structural integrity and reducing deformation during fabrication.

Furthermore, the Au-based inductor coil was characterized through both simulation and experimental measurements, as depicted in Figure 2I,j. The measured inductance of 2.64 μH closely matched the simulated value, validating the coil's design accuracy. Using this inductance value, the simulated initial resonance frequency was determined to be 87 MHz (Figure 2K).

Figure 3A presents the 3D printing setup, which includes the preparation of the PCL/CNT composite and its deposition process. The stent design, incorporating rings and connectors to enhance mechanical reinforcement and flexibility, is shown in Figure 3B. The fabricated PCL/CNT composite stent positioned on the printing shaft is displayed in Figure 3C. The optical images of the fabricated PCL and PCL/CNT hybrid nanocomposite shown in Figure 3D,e. Microscopic images further reveal an improved structural uniformity facilitated by CNT reinforcement. The morphology and dispersion of CNTs within the PCL matrix were examined through FESEM, as depicted in Figure 3F. The FESEM images confirm the homogeneous distribution of CNTs within the polymer matrix with 1%, which plays a crucial role in enhancing load transfer and improving the overall mechanical properties and composite modulus of the stent.[43,44] The FESEM images confirm the homogeneous distribution of CNTs within the polymer matrix, which plays a crucial role in enhancing load transfer and improving the overall mechanical properties of the composite stent. The radial force of the stent, a key parameter in evaluating its ability to withstand vascular pressure and maintain structural integrity, was assessed by measuring the force−displacement relationship. Figure 3G presents the radial force−displacement curves for stents made of PCL, PLA, and PCL/CNT composites. The results indicate that pure PCL exhibits the lowest radial force, which is insufficient for maintaining adequate vascular expansion. PLA demonstrates improved radial force compared to PCL. In contrast, the PCL/CNT composite exhibits the highest radial force, significantly surpassing both PCL and PLA. This enhancement is attributed to the viscoelastic nature of the PCL matrix in combination with the reinforcing effect of the CNT network. The addition of CNTs creates interfacial interactions or agglomerates that impede uniform stress distribution, leading to increased energy dissipation during cyclic loading and unloading. As a result, the PCL/CNT composite displays a more pronounced mechanical hysteresis compared to pure PCL. This behavior is consistent with previous studies, which have reported that certain nanotube configurations in polymer matrices contribute to delayed elastic recovery and higher internal damping.[42] To evaluate the durability of mechanical performance, cyclic testing was conducted on the PCL, PLA, and PCL/CNT BVS samples, as shown in Figure S8. The experimental results indicate that the cyclic force−displacement responses of all three samples remained stable after 10 loading−unloading cycles, confirming their mechanical reliability under repeated deformation. The measured radial force values for each material were 0.013 N/mm for PCL, 0.06 N/mm for PLA, and 0.1 N/mm for the PCL/CNT composite. These findings confirm that incorporating CNTs into PCL significantly enhances its mechanical strength, making it more suitable for

https://doi.org/10.1021/acssensors.5c00857
ACS Sens. XXXX, XXX, XXX−XXX

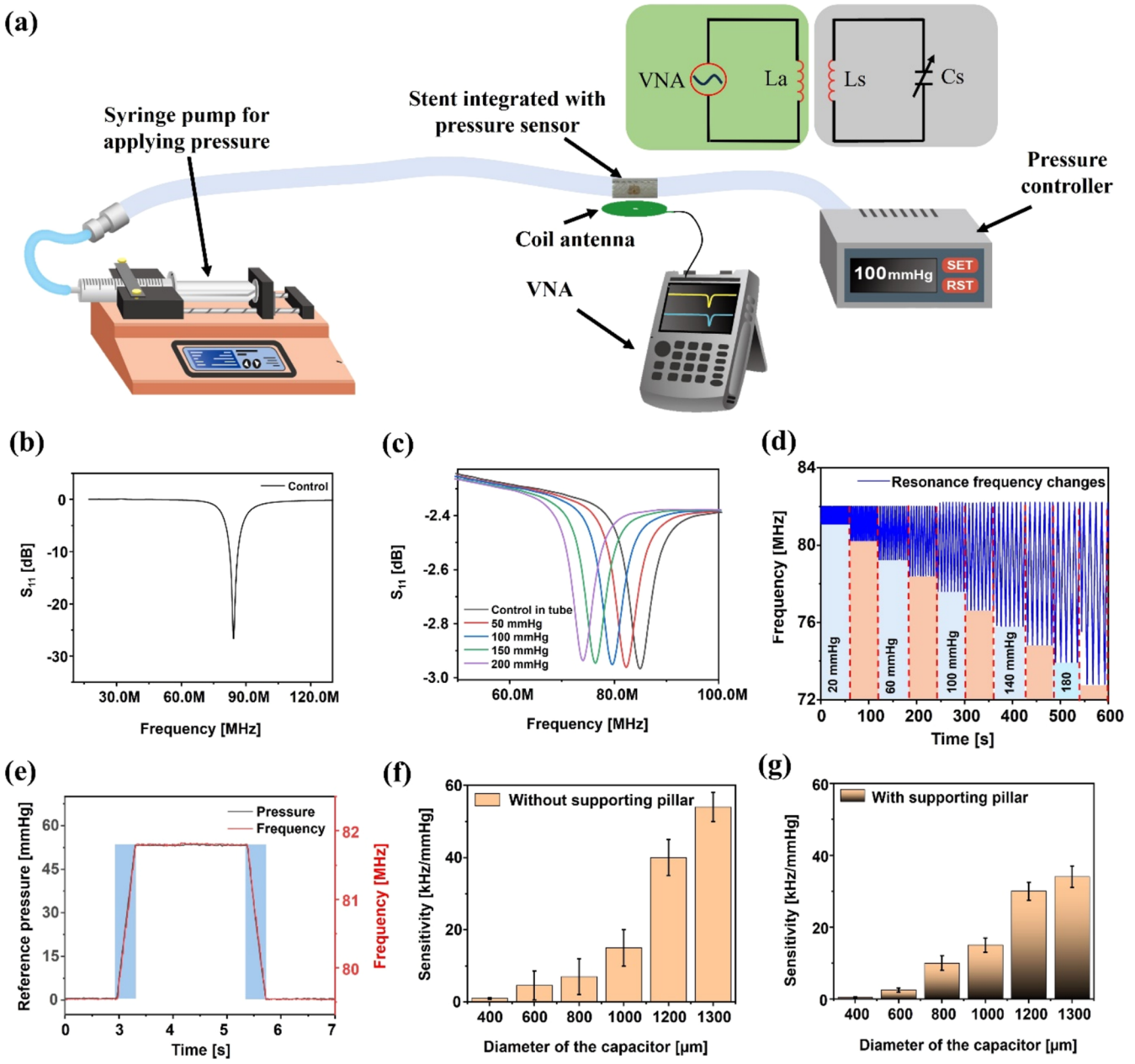

Figure 4. Characterization of the LC pressure sensor under applied pressure conditions. (a) Schematic representation of the experimental setup used for sensor characterization. (b) Initial resonance frequency response of the LC sensor. (c) Capacitive sensor response under different applied pressures (60−200 mmHg). (d) Real-time resonance frequency changes recorded during stepped pressure increments from 0 to 200 mmHg in 20 mmHg intervals. (e) Time-dependent response of the sensor, showing the correlation between applied pressure and resonance frequency. (f, g) Comparison of sensor sensitivity with and without a microsupporting pillar across different capacitor diameters (400−1300 μm).

stent fabrication. To further assess the mechanical performance of the stents, a three-point bending test was conducted to evaluate their flexibility and bending stiffness under applied loading conditions. Figure 3H illustrates the deformation behavior of PCL, PLA, and PCL/CNT composite stents at different loading stages, including before load, maximum load, and release load. The results indicate that PCL stents exhibit the highest flexibility, undergoing significant deformation under applied stress, while PLA stents show moderate flexibility but are prone to brittleness. In contrast, PCL/CNT composite stents demonstrate reduced flexibility while maintaining their structural integrity under bending loads, highlighting their mechanical robustness. The flexibility index was calculated for each material to quantify its ability to withstand bending stress, as shown in Figure 3I. The measured flexibility indices were 8.0 ± 0.05 mm/N for PCL, 5.6 ± 0.03 mm/N for PLA, and 6.8 ± 0.11 mm/N for the PCL/CNT composite. These results suggest that CNT incorporation reduces overall flexibility due to the reinforcing effect of CNTs within the PCL matrix. However, despite the reduction in flexibility, the mechanical strength and durability of the PCL/CNT composite are significantly enhanced, making it a more suitable material for stent applications requiring improved radial strength and long-term stability. A summary of the radial force and stent diameter associated with each material is provided in Table S1, facilitating a comparison between pure

https://doi.org/10.1021/acssensors.5c00857
ACS Sens. XXXX, XXX, XXX−XXX

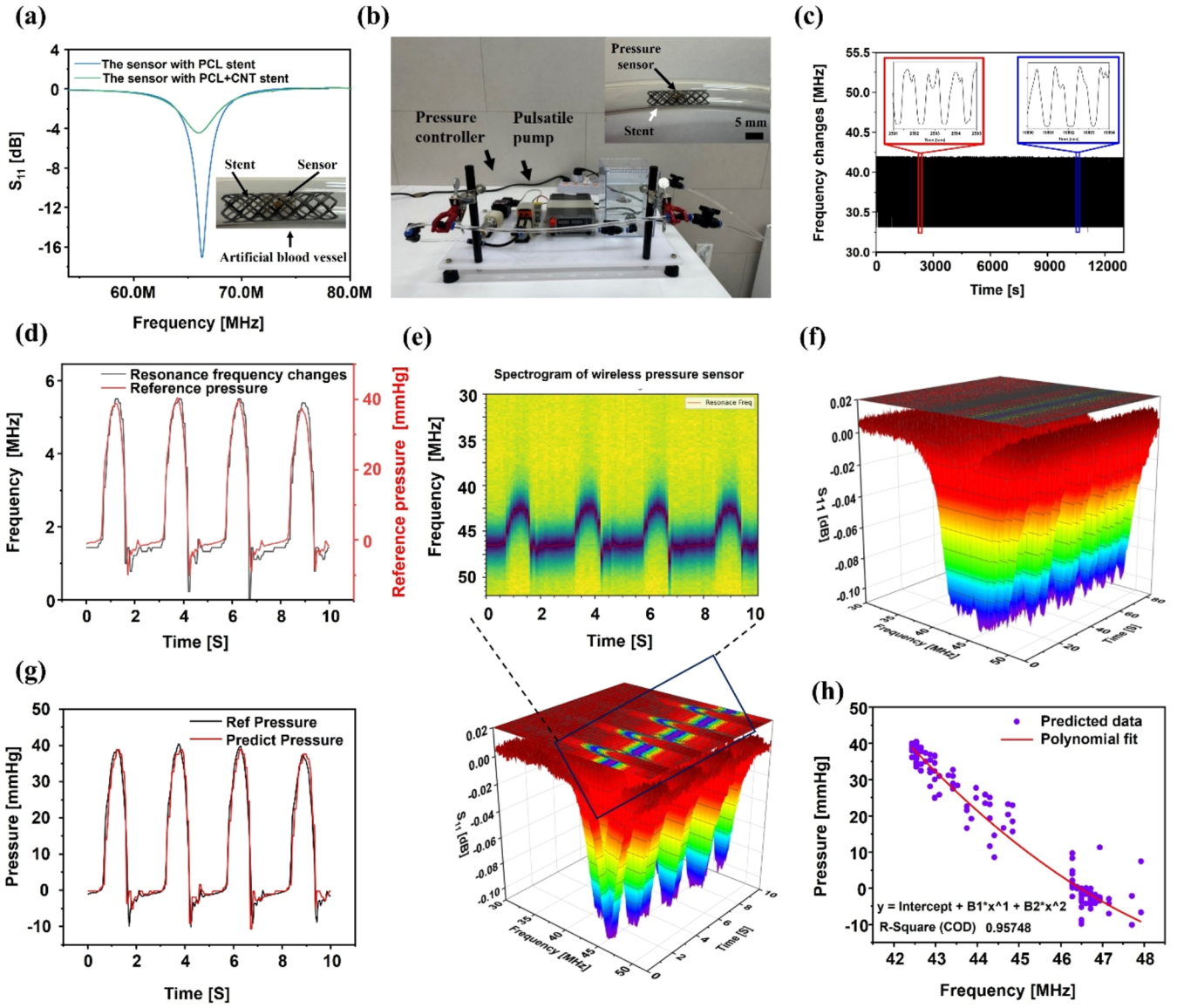

Figure 5. In-vitro evaluation of the 3D-Printed PCL/CNT smart stent using a custom-built phantom system. (a) Resonance frequency response of the LC sensor embedded in PCL and PCL/CNT stents. (b) Experimental setup of the phantom system, incorporating a pulsatile pump, pressure controller, and an artificial blood vessel with the 3D-Printed PCL/CNT smart stent for real-time pressure monitoring. (c) Long-term stability assessment of the sensor monitoring frequency variations over an extended duration. (d) Real-time tracking of resonance frequency shifts in response to dynamic pressure variations, highlighting the correlation between applied pressure and frequency changes. (e, f) Time-frequency spectrograms visualizing resonance frequency fluctuations over short-term (10 s) and long-term (60 s). (g) Comparative analysis of applied reference pressure and predicted pressure values derived from the sensor's resonance frequency response. (h) Polynomial regression analysis of the resonance frequency-pressure relationship, demonstrating a strong correlation (R^2 = 0.96), confirming the sensor's high sensitivity and predictive capability for pressure variations in a in vitro environment.

PCL and PLA-based stents. It is important to note that radial force is strongly influenced by strut thickness. While some PLA-based stents exhibit higher radial force, they also demonstrate brittle behavior, leading to irreversible deformation upon cracking.

The flexibility index was calculated for each material to quantify its ability to withstand bending stress, as shown in Figure 3I. The measured flexibility indices were 8.0 ± 0.05 mm/N for PCL, 5.6 ± 0.03 mm/N for PLA, and 6.8 ± 0.11 mm/N for the PCL/CNT composite. These results suggest that CNT incorporation reduces overall flexibility due to the reinforcing effect of CNTs within the PCL matrix. However, despite the reduction in flexibility, the mechanical strength and durability of the PCL/CNT composite are significantly enhanced, making it a more suitable material for stent applications requiring improved radial strength and long-term stability. A summary of the radial force and stent diameter associated with each material is provided in Table S1, facilitating a comparison between pure PCL and PLA-based stents. It is important to note that radial force is strongly influenced by strut thickness. While some PLA-based stents exhibit higher radial force, they also demonstrate brittle behavior, leading to irreversible deformation upon cracking.

The biocompatibility of the fabricated BVS was assessed by culturing neonatal rat ventricular myocytes (NRVM) on three substrates: a polystyrene dish (control), a PCL stent, and a

https://doi.org/10.1021/acssensors.5c00857
ACS Sens. XXXX, XXX, XXX−XXX

PCL/CNT composite stent. The detailed NRVM procedure is provided in the Supporting Information. Cells were seeded at 1000 cells/mm^2, and their proliferation and morphology were monitored over 9 days to evaluate cytotoxicity. Figure S9 shows optical microscopy images of cell attachment and proliferation at Days 3, 6, and 9. The control group exhibited uniform adhesion and a dense NRVM monolayer. Similarly, cells on PCL and PCL/CNT stents adhered and proliferated without cytotoxicity. At Day 3, initial attachment was comparable across all groups. By Day 6, cells on the control and PCL scaffolds displayed elongated morphology and network formation, indicative of normal cardiomyocyte behavior. A similar trend was observed for PCL/CNT stents, suggesting CNTs did not impair viability. By Day 9, the control group-maintained confluency, while cells on PCL and PCL/CNT scaffolds continued proliferating without detachment or abnormalities. These results confirm that both PCL and PCL/CNT BVS support NRVM adhesion and proliferation, demonstrating biocompatibility for cardiovascular applications.

The pressure-dependent resonance frequency response of the LC pressure sensor was evaluated using a tube designed to mimic artificial blood vessels. The LC pressure sensor integrated with the PCL/CNT BVS was positioned in the middle of the artificial blood vessel. The applied pressure was controlled using a syringe pump and monitored with a commercial pressure sensor (PCM300, Nanjing Wotian Technology, China). The sensor's resonance frequency shifts were measured through inductive coupling, utilizing a coil antenna connected to a Vector Network Analyzer (VNA, N9913B, Keysight Technologies), as shown in Figure 4A. The initial resonance frequency of the sensor was measured at 88 MHz, closely aligning with theoretical and simulation-based predictions (Figure 4B). The sensitivity of the sensor was then characterized under applied pressures ranging up to 200 mmHg, with a stepped pressure increment of 50 mmHg, as shown in Figure 4C. The sensitivity of the sensor was 48 ± 1 kHz/mmHg. The resonance frequency of the capacitor decreased with increasing the applied pressure. The experimental results demonstrated a linear relationship between applied pressure and resonance frequency, confirming the sensor's reliability for real-time pressure monitoring applications.

Figure 4D shows the real-time resonance frequency changes recorded during stepped pressure increments from 0 to 200 mmHg in 20 mmHg intervals. The resonance frequency of the sensor decreased from 82 to 72 MHz as the applied pressure increased from 20 to 200 mmHg, while maintaining a consistent resonance frequency across repeated cyclic measurements, demonstrating the sensor's stability and reliability. The sensor's response time was evaluated by applying and releasing pressure using a syringe pump, and the rise and fall transition times were recorded between 0.7 to 0.8 s, indicating rapid pressure detection (Figure 4E). The sensitivity of the LC pressure sensor integrated PCL stent was further analyzed under different capacitor diameters (400−1300 μm) without and with micropiller structure to assess the impact of a microsupporting pillar in stabilizing the capacitor structure. Figure 4F,G shows the bar graphs that compare the sensor's sensitivity with and without the microsupporting pillar. The results indicate that sensitivity increased with capacitor diameter. However, capacitors without the supporting pillar exhibited higher tolerance variations, attributed to undesirable deformations caused by thermal expansion during fabrication. In contrast, sensor incorporating the microsupporting pillar showed significantly reduced tolerance variations, demonstrating improved mechanical stability.

The structural stability of the sensor was evaluated before and after thermal bonding, as shown in Figure S10. The 2D and 3D surface profiles compare capacitors with and without the microsupporting structure. Prior to bonding, the Perminex cavity layer maintained a uniform 10 μm thickness to ensure consistent capacitor plate spacing. Postbonding, 3D profilometry quantified membrane deformation to assess structural integrity. Without the microsupporting pillar, the capacitor exhibited ∼8 μm downward deflection, leading to increased capacitance variation and higher sensitivity tolerance. In contrast, incorporating the pillar reduced deflection to ∼1 μm, stabilizing the membrane and mitigating deformation. A 1000 μm capacitor showed a sensitivity tolerance of ±20% without the pillar, decreasing to ±5% with its inclusion, demonstrating improved stability. Figure S11 presents optical images of the sensor after bonding, highlighting the inductor side and the flexible capacitor side. These findings indicate a critical trade-off between sensitivity and mechanical stability when incorporating a microsupporting pillar into the sensor design. While the pillar improves structural integrity, enhances durability, and reduces capacitance tolerance variations, it slightly compromises sensitivity, particularly for larger capacitor diameters.

The performance of the LC pressure sensor integrated within the PCL and PCL/CNT BVS was evaluated in a controlled in vitro environment using a custom-built phantom system. Figure 5A presents the resonance frequency response of the sensor embedded in both PCL and PCL/CNT stents, revealing a resonance shift to approximately 68 MHz. This shift represents a decrease of nearly 20 MHz compared to the sensor's initial state (without stent integration), indicating the influence of the stent material on the sensor's inductive and capacitive properties. Notably, the PCL/CNT composite stent exhibited a substantial reduction in S_{11} magnitude, nearly 70%, which can be attributed to the conductive nature of CNTs within the composite structure, enhancing electromagnetic absorption and signal attenuation. The experimental setup for evaluating the sensor's wireless performance is illustrated in Figure 5B. The system comprises a pulsatile pump to generate controlled pressure fluctuations, a commercial pressure sensor for real-time pressure monitoring, and a stent-integrated LC sensor placed within an artificial blood vessel. The entire setup is interfaced with LabVIEW software to ensure precise data acquisition and synchronization of input pressure variations. The sensor's resonance frequency was continuously monitored using a VNA to assess its ability to detect dynamic pressure changes.

To determine the sensor's long-term stability, a continuous measurement was conducted over a duration of 12,000 s with a constant input pressure of 80 mmHg, as shown in Figure 5C. The results demonstrated minimal frequency drift, with the sensor maintaining a stable resonance frequency variation of approximately 1 MHz within the water-filled phantom system. This stability confirms the reliability of the LC sensor for prolonged in vitro measurements, ensuring minimal signal degradation under operational conditions.

The correlation between resonance frequency and applied pressure was further investigated using a regression-based analysis. Figure 5D illustrates real-time frequency shifts in

https://doi.org/10.1021/acssensors.5c00857
ACS Sens. XXXX, XXX, XXX−XXX

response to applied pressure, showing a direct correlation between resonance variations and pressure fluctuations. To enhance data visualization, time-frequency spectrograms were generated over short-term (10 s) and long-term (60 s) intervals, as shown in Figure 5E,f. These spectrograms provide insights into the temporal dynamics of resonance frequency variations, reinforcing the sensor's capability for continuous and accurate pressure monitoring. Machine learning-based regression analysis was employed to further validate the sensor's predictive capability. The reference pressure values were obtained from a commercial pressure sensor and correlated with the recorded resonance frequency shifts to train a predictive model. The trained model was then applied to estimate pressure values based on real-time frequency variations. Figure 5G compares the applied reference pressure with the predicted pressure derived from the sensor's resonance frequency shifts. The results indicate strong agreement between the measured and predicted values, validating the accuracy of the sensor's wireless pressure-sensing mechanism. Figure 5H presents a polynomial regression analysis of the pressure-frequency relationship, demonstrating a strong correlation (R^2 = 0.96). The high coefficient of determination confirms the sensor's predictive capability, showing that machine learning-based regression modeling can effectively map the nonlinear relationship between resonance frequency and applied pressure. These findings highlight the potential of the proposed LC pressure sensor for real-time, wireless vascular pressure monitoring in biomedical applications. The development of a PCL/CNT BVS integrated with a wireless LC pressure sensor represents a significant advancement in cardiovascular implant technology. This innovation addresses the limitations of traditional metallic stents and earlier polymer-based scaffolds by combining enhanced mechanical properties, patient-specific customization, and real-time hemodynamic monitoring. Despite these advancements, certain limitations warrant further investigation. While CNTs offer mechanical advantages, their long-term biocompatibility and potential cytotoxicity remain areas of concern. Although in vitro studies using primary cardiovascular cells have shown promising results, comprehensive in vivo studies and clinical trials are essential to evaluate the long-term safety, efficacy, and performance of the smart stent. Engaging with regulatory bodies early in the development process can facilitate navigation through the approval pathway for novel medical devices.

CONCLUSIONS

To conclude, in this study, we successfully developed a CNT-reinforced PCL BVS with an integrated MEMS-based LC wireless pressure sensor for real-time hemodynamic monitoring. The PCL/CNT stent was fabricated using a 3D printing process, enabling patient-specific customization while significantly enhancing mechanical strength and durability. The wireless pressure sensor, microfabricated using MEMS micromachining techniques, incorporated a supporting micropillar structure, which effectively minimized deformation and ensured a stable capacitance response. Comprehensive mechanical and electrical characterizations confirmed that CNT incorporation significantly improved the stent's radial strength, while the LC sensor demonstrated high sensitivity (49 kHz/mmHg) with minimal capacitance variation (±5%). In vitro evaluations using a custom-built phantom system verified the biocompatibility, structural integrity, and long-term stability of the smart stent. The system enabled continuous, real-time vascular pressure monitoring, facilitating early detection of restenosis and thrombosis without invasive procedures. The proposed smart stent successfully integrated biodegradable nanocomposites, advanced microfabrication, and wireless sensing, marking a significant advancement in cardiovascular implants. By combining structural support with real-time monitoring capabilities, this technology offered a transformative approach to vascular interventions, paving the way for improved patient-specific treatment strategies and better clinical outcomes.

ASSOCIATED CONTENT

Data Availability Statement

The data that support the findings of this study are available from the corresponding author upon reasonable request.

Supporting Information

The Supporting Information is available free of charge at https://pubs.acs.org/doi/10.1021/acssensors.5c00857.

Supplementary tables comparing the mechanical properties of various stent materials; detailed schematic illustrations of PCL/CNT composite preparation, LC sensor fabrication, and integration; SEM and optical images of microfabricated components; cyclic mechanical testing results; biocompatibility evaluation with neonatal rat ventricular myocytes; 2D and 3D surface morphology before and after bonding of the LC pressure sensor; and optical images of the inductor and capacitor parts before and after thermal bonding (PDF)

AUTHOR INFORMATION

Corresponding Author

Dong-Weon Lee − *MEMS and Nanotechnology Laboratory, School of Mechanical Engineering, Chonnam National University, Gwangju 61186, Republic of Korea; Advanced Medical Device Research Center for Cardiovascular Disease and Center for Next-Generation Sensor Research and Development, Chonnam National University, Gwangju 61186, Republic of Korea;* orcid.org/0000-0002-6624-6949; Email: mems@jnu.ac.kr

Authors

Nomin-Erdene Oyunbaatar − *MEMS and Nanotechnology Laboratory, School of Mechanical Engineering, Chonnam National University, Gwangju 61186, Republic of Korea; Advanced Medical Device Research Center for Cardiovascular Disease, Chonnam National University, Gwangju 61186, Republic of Korea*

Jinliang Wei − *MEMS and Nanotechnology Laboratory, School of Mechanical Engineering, Chonnam National University, Gwangju 61186, Republic of Korea; Advanced Medical Device Research Center for Cardiovascular Disease, Chonnam National University, Gwangju 61186, Republic of Korea*

Lei Wang − *MEMS and Nanotechnology Laboratory, School of Mechanical Engineering, Chonnam National University, Gwangju 61186, Republic of Korea; Advanced Medical Device Research Center for Cardiovascular Disease, Chonnam National University, Gwangju 61186, Republic of Korea;* orcid.org/0009-0001-6108-9235

https://doi.org/10.1021/acssensors.5c00857
ACS Sens. XXXX, XXX, XXX−XXX

Su-Hwan Kim − *School of Electrical Engineering, Korea Advanced Institute of Science and Technology, Daejeon 34141, Republic of Korea*
Heonzoo Lee − *Department of Intelligent Electronics and Computer Engineering, Chonnam National University, Gwangju 61186, Republic of Korea*
Kyeongha Kwon − *School of Electrical Engineering, Korea Advanced Institute of Science and Technology, Daejeon 34141, Republic of Korea*
Yonggwan Won − *Department of Intelligent Electronics and Computer Engineering, Chonnam National University, Gwangju 61186, Republic of Korea*

Complete contact information is available at: https://pubs.acs.org/10.1021/acssensors.5c00857

Notes

The authors declare no competing financial interest.

■ ACKNOWLEDGMENTS

This work was supported by the National Research Foundation of Korea (NRF) grant funded by the Korean government (MSIT) (No. RS-2020-NRO49568) and (RS-2022-00165505). We sincerely thank the staff of the MEMS and Nanotechnology Laboratory, School of Mechanical Engineering, Chonnam National University, particularly Kim Do-Ha and Seo Yeongeeol, for their valuable assistance.

■ REFERENCES

(1) Doenst, T.; Haverich, A.; Serruys, P.; Bonow, R. O.; Kappetein, P.; Falk, V.; Velazquez, E.; Diegeler, A.; Sigusch, H. PCI and CABG for treating stable coronary artery disease: JACC review topic of the week. *J. Am. Coll. Cardiol.* **2019**, *73*, 964−976.
(2) Shanmugam, V. B.; Harper, R.; Meredith, I.; Malaiapan, Y.; Psaltis, P. J. An overview of PCI in the very elderly. *J. Geriatr. Cardiol.* **2015**, *12*, 174.
(3) Thiele, H.; Akin, I.; Sandri, M.; Fuernau, G.; de Waha, S.; Meyer-Saraei, R.; Nordbeck, P.; Geisler, T.; Landmesser, U.; Skurk, C.; Fach, A.; et al. PCI strategies in patients with acute myocardial infarction and cardiogenic shock. *N. Engl. J. Med.* **2017**, *377*, 2419−2432.
(4) World Health Organization. Cardiovascular diseases (CVDs). https://www.who.int/news-room/fact-sheets/detail/cardiovascular-diseases-(cvds).
(5) Martin, S. S.; Aday, A. W.; Almarzooq, Z. I.; Anderson, C. A.; Arora, P.; Avery, C. L.; Baker-Smith, C. M.; Barone Gibbs, B.; Beaton, A. Z.; Boehme, A. K.; Commodore-Mensah, Y.; et al. 2024 heart disease and stroke statistics: a report of US and global data from the American Heart Association. *Circulation* **2024**, *149*, e347−e913.
(6) Piccolo, R.; Franzone, A.; Windecker, S. From bare metal to barely anything: an update on coronary stenting. *Heart.* **2018**, *104*, 533−540.
(7) Hong, S. J.; Hong, M. K. Drug-eluting stents for the treatment of coronary artery disease: A review of recent advances. *Expert Opin. Drug Delivery* **2022**, *19*, 269−280.
(8) Majewska, P.; Oledzka, E.; Sobczak, M. Overview of the latest developments in the field of drug-eluting stent technology. *Biomater. Sci.* **2020**, *8*, 544−551.
(9) Ullrich, H.; Olschewski, M.; Muenzel, T.; Gori, T. Coronary in-stent restenosis: predictors and treatment. *Deutsches Ärzteblatt Int.* **2021**, *118*, 637.
(10) Chi, G.; AlKhalfan, F.; Lee, J. J.; Montazerin, S. M.; Fitzgerald, C.; Korjian, S.; Omar, W.; Barnathan, E.; Plotnikov, A.; Gibson, C. M. Factors associated with early, late, and very late stent thrombosis among patients with acute coronary syndrome undergoing coronary stent placement: analysis from the ATLAS ACS 2-TIMI 51 trial. *Front. Cardiovasc. Med.* **2024**, *10*, No. 1269011.
(11) Lin, S.; Dong, P.; Zhou, C.; Dallan, L. A. P.; Zimin, V. N.; Pereira, G. T.; Lee, J.; Gharaibeh, Y.; Wilson, D. L.; Bezerra, H. G.; Gu, L. Degradation modeling of poly-l-lactide acid (PLLA) bioresorbable vascular scaffold within a coronary artery. *Nanotechnol. Rev.* **2020**, *9*, 1217−1226.
(12) Wang, Y.; Zhang, X. Vascular restoration therapy and bioresorbable vascular scaffold. *Regen. Biomat.* **2014**, *1*, 49−55.
(13) Zhao, J.; Song, G.; Zhao, Q.; Feng, H.; Wang, Y.; Anderson, J. M.; Zhao, H.; Liu, Q. Development of three-dimensionally printed vascular stents of bioresorbable poly (l-lactide-co-caprolactone). *J. Biomed. Mater. Res.* **2023**, *111*, 656−664.
(14) Wei, J.; Oyunbaatar, N. E.; Jeong, Y. J.; Park, J.; Kim, S. H.; Kwon, K.; Lee, H.; Won, Y.; Kim, D. S.; Lee, D. W. Enhancing flexibility of smart bioresorbable vascular scaffolds through 3D printing using polycaprolactone and polylactic acid. *Sens. Actuator B-Chem.* **2025**, *422*, No. 136667.
(15) Hussain, M.; Khan, S. M.; Shafiq, M.; Abbas, N. A review on PLA-based biodegradable materials for biomedical applications. *Giant* **2024**, *18*, No. 100261.
(16) DeStefano, V.; Khan, S.; Tabada, A. Applications of PLA in modern medicine. *Eng. Regen.* **2020**, *1*, 76−87.
(17) Khalaj Amnieh, S.; Mosaddegh, P.; Mashayekhi, M.; Kharaziha, M. Biodegradation evaluation of poly (lactic acid) for stent application: Role of mechanical tension and temperature. *J. Appl. Polym. Sci.* **2021**, *138*, 50389.
(18) Ahuja, R.; Kumari, N.; Srivastava, A.; Bhati, P.; Vashisth, P.; Yadav, P. K.; Jacob, T.; Narang, R.; Bhatnagar, N. Biocompatibility analysis of PLA based candidate materials for cardiovascular stents in a rat subcutaneous implant model. *Acta Histochem.* **2020**, *122*, No. 151615.
(19) Malikmammadov, E.; Tanir, T. E.; Kiziltay, A.; Hasirci, V.; Hasirci, N. PCL and PCL-based materials in biomedical applications. *J. Biomate. Sci.- Polym. Ed.* **2018**, *29*, 863−893.
(20) Ang, H. Y.; Huang, Y. Y.; Lim, S. T.; Wong, P.; Joner, M.; Foin, N. Mechanical behavior of polymer-based vs. metallic-based bioresorbable stents. *J. Thorac. Dis.* **2017**, *9*, S923.
(21) Fang, S. Assessing the functional mechanical properties of polycaprolactone stents post-processed by ultrasonic strengthening. *J. Manuf. Process.* **2024**, *118*, 154−162.
(22) Sousa, A. M.; Amaro, A. M.; Piedade, A. P. Structural design optimization through finite element analysis of additive manufactured bioresorbable polymeric stents. *Mater. Today Chem.* **2024**, *36*, No. 101972.
(23) Bhati, P.; Kumar, A.; Bhatnagar, N. Radial strength comparison of the PLA/PCL blends tubes manufactured by different fabrication processes. *Front. Bioeng. Biotechnol. Conference Abstract: 10th World Biomaterials Congress* **2016**, 580.
(24) binti Hashim, H.; binti Emran, N. A. A.; Isono, T.; Katsuhara, S.; Ninoyu, H.; Matsushima, T.; Yamamoto, T.; Borsali, R.; Satoh, T.; Tajima, K. Improving the mechanical properties of polycaprolactone using functionalized nanofibrillated bacterial cellulose with high dispersibility and long fiber length as a reinforcement material. *Compos. Pt. A-Appl. Sci. Manuf.* **2022**, *158*, No. 106978.
(25) Tan, Q.; Mao, C.; Hao, X.; Tao, Y.; Gong, X. Synergistic Effects of Surface-Modified Glass Fiber on Polylactic Acid Matrix Composites Reinforcement and Toughening. *J. Appl. Polym. Sci.* **2025**, *142*, e56744.
(26) Yue, C.; Hua, M.; Li, H.; Liu, Y.; Xu, M.; Song, Y. Printability, shape-memory, and mechanical properties of PHB/PCL/CNFs composites. *J. Appl. Polym. Sci.* **2021**, *138*, 50510.
(27) Guerra, A. J.; Cano, P.; Rabionet, M.; Puig, T.; Ciurana, J. 3D-printed PCL/PLA composite stents: Towards a new solution to cardiovascular problems. *Materials* **2018**, *11*, 1679.
(28) Misra, S. K.; Ostadhossein, F.; Babu, R.; Kus, J.; Tankasala, D.; Sutrisno, A.; Walsh, K. A.; Bromfield, C. R.; Pan, D. 3D-printed multidrug-eluting stent from graphene-nanoplatelet-doped biodegradable polymer composite. *Adv. Healthcare Mater.* **2017**, *6*, No. 1700008.

(29) Zhang, Q.; Wang, M.; Ao, H.; Luo, H.; Deng, X.; Wan, Y. Embedding carbon nanotube to the surfaces of poly (ε-caprolactone) film for multi-responsive actuations. *Polym. Test.* **2021**, *96*, No. 107086.
(30) Abdal-hay, A.; Taha, M.; Mousa, H. M.; Bartnikowski, M.; Hassan, M. L.; Dewidar, M.; Ivanovski, S. Engineering of electrically-conductive poly (ε-caprolactone)/multi-walled carbon nanotubes composite nanofibers for tissue engineering applications. *Ceram. Int.* **2019**, *45*, 15736−15740.
(31) Kim, M.; Kim, Y. B.; Chun, H. J. Effects of iron oxide and carbon nanotube contents on mechanical properties and shape memory behavior of biocompatible and biodegradable shape memory polymers. *Polym. Adv. Technol.* **2024**, *35*, No. e6257.
(32) Shar, A.; Shar, A.; Joung, D. Carbon nanotube nanocomposite scaffolds: advances in fabrication and applications for tissue regeneration and cancer therapy. *Front. Bioeng. Biotechnol.* **2023**, *11*, No. 1299166.
(33) Sánchez-Romate, X. F.; Alvarado, A.; Jiménez-Suárez, A.; Prolongo, S. G. Carbon nanotube reinforced poly (ε-caprolactone)/epoxy blends for superior mechanical and self-sensing performance in multiscale glass fiber composites. *Polymers* **2021**, *13*, 3159.
(34) Jeong, Y. J.; Jeong, S.; Kim, S.; Kim, H.; Jo, J.; Shanmugasundaram, A.; Kim, H.; Choi, E.; Lee, D. W. 3D-printed cardiovascular polymer scaffold reinforced by functional nanofiber additives for tunable mechanical strength and controlled drug release. *Chem. Eng. J.* **2023**, *454*, No. 140118.
(35) Veerubhotla, K.; Lee, C. H. Design of biodegradable 3D-printed cardiovascular stent. *Bioprinting* **2022**, *26*, No. e00204.
(36) Park, J.; Kim, J. K.; Kim, D. S.; Shanmugasundaram, A.; Park, S. A.; Kang, S.; Kim, S. H.; Jeong, M. H.; Lee, D. W. Wireless pressure sensor integrated with a 3D printed polymer stent for smart health monitoring. *Sens. Actuator. B- Chem.* **2019**, *280*, 201−209.
(37) Oyunbaatar, N. E.; Shanmugasundaram, A.; Kwon, K.; Lee, D. W. Continuous monitoring of cardiovascular function with a smart stent incorporating a flexible and stretchable wireless pressure sensor. *J. Micromech. Microeng.* **2023**, *33*, No. 115001.
(38) Wang, L.; Oyunbaatar, N. E.; Jeong, Y. J.; Lee, H.; Won, Y.; Jeong, I. S.; Kayumov, M.; Obiweluozor, F. O.; Kim, D. S.; Lee, D. W. The PolyCraft Polymer−Metal Hybrid Smart Stent System: The Future of Cardiovascular Blood Pressure Management. *Adv. Funct. Mater.* **2024**, *34*, No. 2408022.
(39) Sun, G. H.; Kim, D. S.; Shanmugasundaram, A.; Lee, D. W. Additive manufactured cardiovascular scaffold integrated with SU-8 based wireless pressure sensor. *J. Micromech. Microeng.* **2022**, *32*, No. 115003.
(40) Oyunbaatar, N. E.; Kim, D. S.; Shanmugasundaram, A.; Kim, S. H.; Jeong, Y. J.; Jo, J.; Kwon, K.; Choi, E.; Lee, D. W. Implantable Self-Reporting Stents for Detecting In-Stent Restenosis and Cardiac Functional Dynamics. *ACS Sens* **2023**, *8*, 4542−4553.
(41) Shi, R.; Ye, D.; Ma, K.; Tian, W.; Zhao, Y.; Guo, H.; Ritchie, R. O.; et al. Understanding the interfacial adhesion between natural silk and polycaprolactone for fabrication of continuous silk biocomposites. *ACS Appl. Mater. Interfaces* **2022**, *14*, 46932−46944.
(42) Gumede, T. P.; Luyt, A. S.; Muller, A. J. Review on PCL, PBS, and PCL/PBS blends containing carbon nanotubes. *Express Polym. Lett.* **2018**, *12*, 505−529.
(43) Wu, Z.; Zhao, Y.; Yang, K.; Guan, J.; Wang, S.; Gu, Y.; Ritchie, R. O.; et al. Enhancing the mechanical performance of fiber-reinforced polymer composites using carbon nanotubes as an effective nano-phase reinforcement. *Adv. Mater. Interfaces* **2023**, *10*, No. 2201935.
(44) Pantano, A. Mechanical properties of CNT/polymer. In *Carbon Nanotube-Reinforced Polymers*; Elsevier, 2018; pp 201−232.

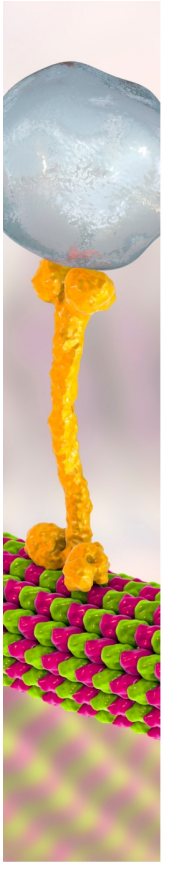

https://doi.org/10.1021/acssensors.5c00857
ACS Sens. XXXX, XXX, XXX−XXX